
SITReg: Multi-resolution architecture for symmetric, inverse consistent, and topology preserving image registration using deformation inversion layers

Joel Honkamaa
 Department of Computer Science
 Aalto University
 Aalto, Finland
 joel.honkamaa@aalto.fi

Pekka Marttinen
 Department of Computer Science
 Aalto University
 Aalto, Finland
 pekka.marttinen@aalto.fi

Abstract

Deep learning based deformable medical image registration methods have emerged as a strong alternative for classical iterative registration methods. Since image registration is in general an ill-defined problem, the usefulness of inductive biases of symmetricity, inverse consistency and topology preservation has been widely accepted by the research community. However, while many deep learning registration methods enforce these properties via loss functions, no prior deep learning registration method fulfills all of these properties by construct. Here, we propose a novel multi-resolution registration architecture which is by construct symmetric, inverse consistent, and topology preserving. We also develop an implicit layer for memory efficient inversion of the deformation fields. The proposed method achieves state-of-the-art registration accuracy on two datasets.

1 Introduction

We study deformable medical image registration using deep learning, where the goal is to find a mapping between coordinate systems of two images to match the corresponding anatomical parts. The predicted coordinate mappings are called deformations. Typically, deep learning is applied by training a registration network which outputs a candidate deformation for two input images. We focus on unsupervised intra-modality registration, where there is no ground truth deformation and the images are of the same modality, which is useful, e.g., when deforming brain MRI images from different patients to an atlas or analyzing a patient’s breathing cycle using multiple images. Since medical image registration is challenging, various properties are often assumed to improve the registration quality: *inverse consistency*, *symmetry*, and *topology preservation*, are widely seen as useful by the research community (Sotiras et al., 2013). Another property is diffeomorphism, which however overlaps with topology preservation, and hence we consider them as one, as explained later. Although these properties do not guarantee successful registration, they serve as inductive biases to narrow down the search space. As terminology in the literature can be ambiguous, we begin by precisely defining each property, and we provide further clarifications of them in Appendix X.

We define a *registration method* as a function f that takes two images, x_1 and x_2 , and produces a deformation. Some methods can output the deformation in both directions, and we use subscripts to indicate the direction. For example, $f_{1 \rightarrow 2}$ produces a deformation that aligns the image of the first argument to the image of the second argument. As a result, a registration method may predict up to four different deformations for any given input pair: $f_{1 \rightarrow 2}(x_1, x_2)$, $f_{2 \rightarrow 1}(x_1, x_2)$, $f_{1 \rightarrow 2}(x_2, x_1)$, and $f_{2 \rightarrow 1}(x_2, x_1)$. Some methods predict deformations in one direction only, resulting in two possible outputs: $f_{1 \rightarrow 2}(x_1, x_2)$ and $f_{1 \rightarrow 2}(x_2, x_1)$, in which case we might omit the subscript.

Inverse consistent registration methods ensure that $f_{1 \rightarrow 2}(x_1, x_2)$ is an accurate inverse of $f_{2 \rightarrow 1}(x_1, x_2)$, which we quantify using the *inverse consistency error*: $\|f_{1 \rightarrow 2}(x_1, x_2) \circ f_{2 \rightarrow 1}(x_1, x_2) - \mathcal{I}\|^2$, where \circ is the composition operator and \mathcal{I} is the identity deformation. Originally inverse consistency was achieved via variational losses (Christensen et al., 1995) but later algorithms were *inverse consistent by construct*, e.g., classical methods DARTEL (Ashburner, 2007) and SyN (Avants et al., 2008). However, due to a limited spatial resolution of the predicted deformations, even for these methods the inverse consistency error is not exactly zero. Some deep learning methods enforce inverse consistency via a penalty (Zhang, 2018; Kim et al., 2019; Estienne et al., 2021). A popular stationary velocity field (SVF) formulation Arsigny et al. (2006) achieves inverse consistency by construct and has been used by many works, e.g. Dalca et al. (2018); Krebs et al. (2018, 2019); Niethammer et al. (2019); Shen et al. (2019a,b); Mok and Chung (2020a).

In *symmetric registration*, the registration outcome does not depend on the order of the inputs, i.e., $f_{1 \rightarrow 2}(x_1, x_2)$ equals $f_{2 \rightarrow 1}(x_2, x_1)$. Since anatomical correspondence trivially does not depend on the input order, enforcing the property is very natural. Unlike with inverse consistency, $f_{1 \rightarrow 2}(x_1, x_2)$ can equal $f_{2 \rightarrow 1}(x_2, x_1)$ exactly for some methods (Avants et al., 2008; Estienne et al., 2021), which we call *symmetric by construct*. A related property, cycle consistency, can be assessed using *cycle consistency error* $\|f(x_1, x_2) \circ f(x_2, x_1) - \mathcal{I}\|^2$. It can be computed for any method since it does not require the method to predict deformations in both directions. If the method is symmetric by construct, inverse consistency error equals cycle consistency error. Some existing deep learning registration methods enforce cycle consistency (Mahapatra and Ge, 2019; Gu et al., 2020; Zheng et al., 2021) via a penalty. The method by Estienne et al. (2021) is symmetric by construct but only for a single component of their multi-step formulation, and also it is not inverse consistent by construct making the symmetry less powerful. Very recently in parallel to us, Iglesias (2023) proposed a by construct symmetric and inverse consistent registration method within the SVF framework. The work had no effect on our work and achieved the goal in a way different from ours.

The third property, *topology preservation* of predicted deformations, we define similarly to Christensen et al. (1995). From the real-world point of view it refers to the preservation of anatomical structures. Mathematically we want the deformations to be homeomorphisms, i.e., invertible and continuous. In registration literature it is common to talk about diffeomorphisms which are additionally differentiable. In practice we want a deformation not to fold on top of itself which we measure by estimating the local Jacobian determinants of the predicted deformations and checking whether they are positive. Most commonly in deep learning applications topology preservation is achieved using the diffeomorphic SVF formulation (Arsigny et al., 2006). It does not completely prevent the deformation from folding but such voxels are usually limited to just a handful in the whole volume of millions of voxels, which is usually sufficient in practice. Topology preservation can also be encouraged using a specific loss, e.g. by penalizing negative determinants (Mok and Chung, 2020a).

Our main contributions can be summed up as follows:

- We propose a multi-resolution deep learning registration architecture which is by construct inverse consistent and symmetric, and preserves topology. The properties are fulfilled for the whole multi-resolution pipeline, not just separately for each resolution. Apart from the parallel work (Iglesias, 2023), we are not aware of other deep learning registration methods which are by construct both symmetric and inverse consistent, and ours is the first such method with a multi-resolution deep learning architecture. For motivation of the multi-resolution approach, see Section 2.2.
- As a component in our architecture, we propose an *implicit* neural network layer, which we call *deformation inversion layer*, based on a well-known fixed point iteration formula (Chen et al., 2008) and recent advances in Deep Equilibrium models (Bai et al., 2019; Duvenaud et al., 2020). The layer allows memory efficient inversion of deformation fields.
- We show that the method achieves state-of-the-art results on two popular benchmark data sets in terms of registration accuracy and deformation regularity. The accuracy of the inverses generated by our method is also very good and similar to the s-o-t-a SVF framework.

We name the method *SITReg* after its symmetricity, inverse consistency and topology preservation properties.

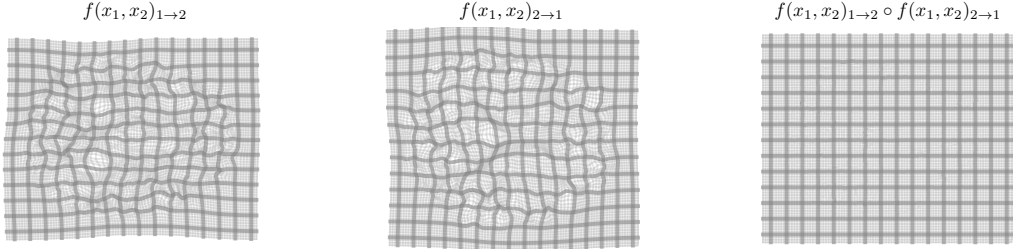


Figure 1: **Example deformation produced by the method.** Composition of the forward and the inverse deformations is shown on the right to demonstrate the accuracy of the inverse. Only one 2D slice is shown of the 3D deformation. The visualized deformation is from the LPBA40 experiment.

2 Preliminaries

2.1 Topology preserving registration

The LDDMM method by (Cao et al., 2005) is a classical registration method that can generate diffeomorphic deformations which preserve topology, but it has not been used much in deep learning due to computational cost. Instead, a simpler stationary velocity field (SVF) method (Arsigny et al., 2006) has been popular (Krebs et al., 2018, 2019; Niethammer et al., 2019; Shen et al., 2019a,b; Mok and Chung, 2020a). In SVF the final deformation is obtained by integrating a stationary velocity field over itself over a unit time, which under mild continuity constraints for the velocity field results in a diffeomorphism. Another classical method by Choi and Lee (2000); Rueckert et al. (2006) uses a different approach to generate invertible deformations. The idea is to constrain a deformation to be diffeomorphic but small, and to form the final deformation as a composition of multiple such small deformations. Since diffeomorphisms form a group under composition, also the final deformation is diffeomorphic. Note that this is actually close to a practical implementation of the SVF, where the velocity field is usually integrated by first scaling the velocity field down by a power of two and interpreting the result as a small deformation, which is then repeatedly composed with itself for the final deformation. The idea is hence similar: a composition of small deformations.

In this work we build topology preserving deformations using the same strategy: as composition of small topology preserving deformations.

2.2 Multi-resolution registration

Multi-resolution registration methods learn the deformation by first estimating it in a low resolution and then incrementally improving it while moving towards higher a resolution. For each resolution one feeds the inputs deformed with the deformation learned thus far, and incrementally composes the full deformation. The approach has been around for already a few decades (Rueckert et al., 1999; Oliveira and Tavares, 2014) and has been used by many methods, including the top-performing classical and deep learning registration methods (Avants et al., 2008; Klein et al., 2009; Mok and Chung, 2020b, 2021; Hering et al., 2022).

In this work we propose the first multi-resolution deep learning registration architecture that is by construct symmetric, inverse consistent, and topology preserving.

2.3 Symmetric registration formulations

Symmetric registration does not assign moving or fixed identity to either image but instead considers them equally. A classical registration method called symmetric normalization (SyN) Avants et al. (2008) proposed a symmetric registration algorithm which learns two separate transformations: one for deforming the first image half-way toward the second image and the other for deforming the second image half-way toward the first image. The images are then matched in the intermediate coordinates and the full deformation can be obtained as composition of the half-way deformations (of which either one is inverted). The idea of matching the images in intermediate coordinates has later been used by other methods such as the deep learning method SYMNet Mok and Chung (2020a). However, SYMNet does not guarantee symmetry by construct for individual predictions.

In our architecture we use the intuition of deforming the images half-way towards each other to achieve inverse consistency and symmetry throughout our multi-resolution architecture.

2.4 Deep equilibrium networks

Deep equilibrium networks use *implicit* fixed point iteration layers, which have emerged as an alternative to the common *explicit* layers in deep learning (Bai et al., 2019, 2020; Duvenaud et al., 2020). Unlike explicit layers, which produce output via an exact sequence of operations, the output of an implicit layer is defined indirectly as a solution to a fixed point equation, which in turn is defined using a fixed point mapping. In the simplest case the fixed point mapping takes two arguments, one of which is the input. For example, let $g : A \times B \rightarrow B$ be a fixed point mapping defining an implicit layer. Then, for some input a , the output of the layer is a solution z for equation

$$z = g(z, a). \quad (1)$$

Such an equation is called a fixed point equation and the solution is called a fixed point solution. If g has suitable properties, the equation can be solved iteratively by starting with an initial guess and repeatedly feeding the output as the next input to g . More advanced iteration methods have also been developed for solving fixed point equations, such as Anderson acceleration (Walker and Ni, 2011).

The main mathematical innovation related to deep equilibrium networks is that the derivative of such a layer with respect to its inputs can be calculated based solely on a fixed point solution, i.e., no intermediate iteration values need to be stored for back-propagation. Now given some, solution (a_0, z_0) , such that $z_0 = g(z_0, a_0)$, and assuming certain local invertibility properties for g , the implicit function theorem ensures the existence of a solution mapping in the neighborhood of the solution (a_0, z_0) , which for another input outputs another solution to the fixed point equation. Let us denote the solution mapping as z^* . The solution mapping can be seen as the theoretical explicit layer corresponding to the implicit layer. To find the derivatives of the implicit layer we need to find the Jacobian of z^* at point a_0 which can be obtained using implicit differentiation as

$$\partial z^*(a_0) = [I - \partial_1 g(z_0, a_0)]^{-1} \partial_0 g(z_0, a_0).$$

The vector-Jacobian product of z^* needed for neural network back-propagation can be calculated from this using another fixed point equation, without fully computing the Jacobians, see, e.g., Duvenaud et al. (2020). As a result, both forward and backward passes of the fixed point iteration layer can be computed as a fixed point iteration.

We use these ideas to develop a neural network layer for inverting deformations based on the fixed point equation proposed for that by Chen et al. (2008). The resulting layer is very memory efficient as only the fixed point solution needs to be stored for the backward pass.

3 Methods

In deformable image registration the goal is to find a mapping from \mathbb{R}^n to \mathbb{R}^n , connecting the coordinate systems of two non-aligned images $x_1, x_2 : \mathbb{R}^n \rightarrow \mathbb{R}^k$, often called a deformation. Here n is the dimensionality of the image, e.g. $n = 3$ for three dimensional medical images, and k is the number of channels, e.g. $k = 3$ for an RGB-image. Mathematically a deformation applied to an image can be represented as a composition of the image with the deformation, denoted by \circ , and in practice we use linear interpolation to represent images in continuous coordinates. Similarly to many works in image registration, we want to learn a *neural network* f that can take two images as input and output the deformation connecting the image coordinates. That is, we would like in some sense that $x_1 \circ f(x_1, x_2) \approx x_2$, which in the medical context refers to anatomical correspondence.

3.1 Symmetric formulation

As discussed in the introduction Section 1, we want our method to be symmetric. To achieve this, we propose to define the network f using an auxiliary network u , which also predicts deformations, as

$$f(x_1, x_2) := u(x_1, x_2) \circ u(x_2, x_1)^{-1} \quad (2)$$

As a result, it holds that $f(x_1, x_2) = f(x_2, x_1)^{-1}$ apart from errors introduced by the composition and inversion, meaning that the cycle-consistency error should be very small. An additional benefit

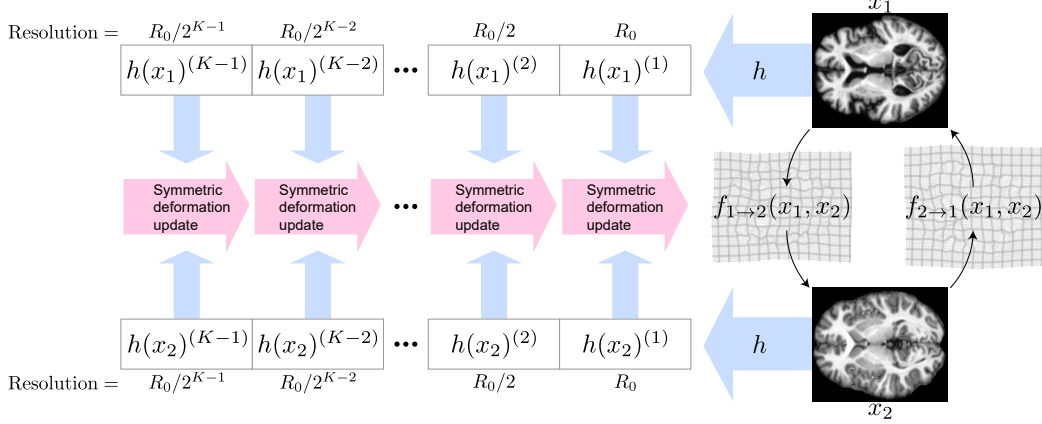


Figure 2: **Overview of the proposed architecture.** Multi-resolution features are first extracted from the inputs x_1 and x_2 using convolutional encoder h . Output deformations $f_{1 \rightarrow 2}(x_1, x_2)$ and $f_{2 \rightarrow 1}(x_1, x_2)$ are built recursively from the multi-resolution features using the symmetric deformation updates described in Section 3.2 and visualized in Figure 3.2. The architecture is symmetric and inverse consistent with respect to the inputs and the final deformation is obtained in both directions. The brain images are from the OASIS dataset (Marcus et al., 2007)

is that $f(x_1, x_1)$ should equal the identity transformation, again apart from numerical inaccuracies, which is a very natural property for a registration method. Applying the formulation in Equation 2 naively would double the computational cost. Hence we propose to encode features from both the inputs separately before feeding them to the deformation extraction network following Equation 2. Extracting features separately has been used in recent registration methods (Estienne et al., 2021; Young et al., 2022). Denoting the feature extraction network by h , the modified formulation is

$$f(x_1, x_2) := u(h(x_1), h(x_2)) \circ u(h(x_2), h(x_1))^{-1}. \quad (3)$$

3.2 Multi-resolution architecture

As the overarching architecture, we propose a novel symmetric and inverse consistent multi-resolution coarse-to-fine approach. For motivation, see Section 2.2. Overview of the whole architecture is visualized in Figure 3.2. First, we extract image feature representations $h^{(k)}(x_1), h^{(k)}(x_2)$, at different resolutions $k \in \{0, \dots, K-1\}$. Index $k=0$ is the original resolution and increasing k by one halves the spatial resolution. In practice h is a ResNet (He et al., 2016) style convolutional network. Starting from the lowest resolution $k=K-1$, we recursively build the final deformation between the inputs using the extracted feature representations. To ensure symmetry, we build two deformations: one for deforming the first image half-way towards the second image, and the other for deforming the second image half-way towards the first image (see Section 2.3). The full deformation is then composed of these at the final stage. Let us denote the half-way deformations extracted at resolution k as $f_{1 \rightarrow 1.5}^{(k)}(x_1, x_2)$ and $f_{2 \rightarrow 1.5}^{(k)}(x_1, x_2)$. Initially, at level $k=K$, these are identity deformations. Then, at each $k=K-1, \dots, 0$, the half-way deformations are updated by composing them with a predicted update deformation. In detail, the update at level k consists of three steps (visualized in Figure 3.2):

1. Deform the feature representations $h^{(k)}(x_1), h^{(k)}(x_2)$ of level k towards each other by the half-way deformations from the previous level $k+1$:

$$\begin{cases} z_1^{(k)} := h^{(k)}(x_1) \circ f_{1 \rightarrow 1.5}^{(k+1)}(x_1, x_2) \\ z_2^{(k)} := h^{(k)}(x_2) \circ f_{2 \rightarrow 1.5}^{(k+1)}(x_1, x_2) \end{cases} \quad (4)$$

2. Define an update deformation $U^{(k)}$, using the idea from Equation 3 and the half-way deformed feature representations $z_1^{(k)}$ and $z_2^{(k)}$:

$$U^{(k)} := u^{(k)}(z_1^{(k)}, z_2^{(k)}) \circ u^{(k)}(z_2^{(k)}, z_1^{(k)})^{-1}. \quad (5)$$

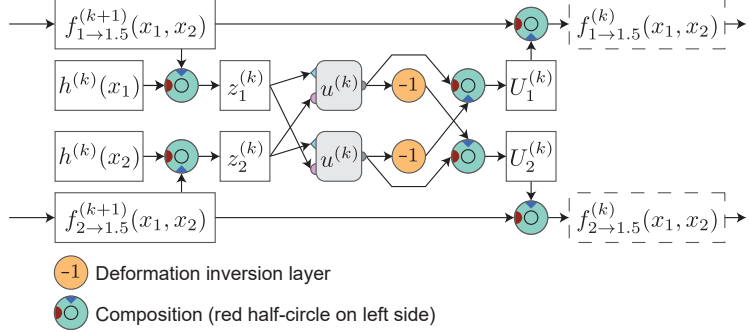


Figure 3: **Recursive multi-resolution deformation update.** Figure visualizes the deformation update at resolution k , described in Section 3.2. The update takes as input the half-way deformations $f_{1 \rightarrow 1.5}^{(k+1)}(x_1, x_2)$ and $f_{2 \rightarrow 1.5}^{(k+1)}(x_1, x_2)$ from the previous resolution, and updates them through a composition with an update deformation $U^{(k)}$. $U^{(k)}$ is calculated symmetrically from image features $z_1^{(k)}$ and $z_2^{(k)}$ at resolution k (deformed mid-way towards each other with the previous half-way deformations), using a neural network $u^{(k)}$ according to Equation 5. The deformation inversion layer is used to invert the auxiliary deformations predicted by $u^{(k)}$ and it is described in Section 3.3.

Here, $u^{(k)}$ is a trainable convolutional neural network (details in Appendix I) predicting an auxiliary deformation. The intuition here is that the symmetrically predicted update deformation $U^{(k)}$ should learn to adjust for whatever differences in the image features remain after deforming them half-way towards each other in Step 1 with deformations $f^{(k+1)}$ from the previous resolution.

3. Obtain the updated half-way deformation $f_{1 \rightarrow 1.5}^{(k)}(x_1, x_2)$ by composing the earlier half-way deformation of level $k + 1$ with the update deformation $U^{(k)}$

$$f_{1 \rightarrow 1.5}^{(k)}(x_1, x_2) = f_{1 \rightarrow 1.5}^{(k+1)}(x_1, x_2) \circ U^{(k)}. \quad (6)$$

For the other direction $f_{2 \rightarrow 1.5}^{(k)}(x_1, x_2)$, we use the inverse of the deformation update $(U^{(k)})^{-1}$ which can be obtained simply by reversing $z_1^{(k)}$ and $z_2^{(k)}$ in Equation 5:

$$f_{2 \rightarrow 1.5}^{(k)}(x_1, x_2) = f_{2 \rightarrow 1.5}^{(k+1)}(x_1, x_2) \circ (U^{(k)})^{-1}. \quad (7)$$

The inverses $f_{1 \rightarrow 1.5}^{(k)}(x_1, x_2)^{-1}$ and $f_{2 \rightarrow 1.5}^{(k)}(x_1, x_2)^{-1}$ are updated similarly.

The full deformations are obtained at stage $k = 0$ as:

$$\begin{cases} f_{1 \rightarrow 2}(x_1, x_2) &= f_{1 \rightarrow 1.5}^{(0)}(x_1, x_2) \circ f_{2 \rightarrow 1.5}^{(0)}(x_1, x_2)^{-1} \\ f_{2 \rightarrow 1}(x_1, x_2) &= f_{2 \rightarrow 1.5}^{(0)}(x_1, x_2) \circ f_{1 \rightarrow 1.5}^{(0)}(x_1, x_2)^{-1} \end{cases} \quad (8)$$

The motivation to use half-way deformations is that if we instead used learned full deformations at each stage, we would have to decide either of the image coordinates to which to deform the feature representations of the next stage, which would break the symmetry of the overall architecture. Now we can instead deform the feature representations of both of the inputs by the symmetrically predicted half-way deformations, which ensures that the updated deformations from each stage are separately invariant to input order.

Proposition 3.1. *The proposed multi-resolution architecture is by construct symmetric and inverse consistent.*

Proof. Appendix IV, including also discussion on numerical errors from compositions and inversions.

3.3 Implicit deformation inversion layer

Implementing the architecture requires inverting deformations from $u^{(k)}$ in Equation 5. This could be done, e.g., with the SVF framework, but we propose an approach which requires storing 5 times less data for backward pass compared to the standard SVF, resulting in significant memory saving due to the large number of inversions required. For details on memory usage see Appendix VI.

As shown by Chen et al. (2008), deformations can be inverted in certain cases by a fixed point iteration. Consequently, we propose to use the deep equilibrium network framework from Section 2.4 for inverting deformations, and label the resulting layer *deformation inversion layer*. The fixed point equation proposed by Chen et al. (2008) is

$$g(z, a) := -(a - \mathcal{I}) \circ z + \mathcal{I},$$

where a is the deformation to be inverted, z is the candidate for the inverted a , and \mathcal{I} is the identity deformation. It is easy to see that feeding a^{-1} for z , yields a^{-1} as an output. We use Anderson acceleration (Walker and Ni, 2011) for solving the fixed point equation and use the memory-efficient back-propagation (Bai et al., 2019; Duvenaud et al., 2020) strategy discussed in Section 2.4.

Lipschitz condition is sufficient but not necessary for the fixed point algorithm to converge (Chen et al., 2008). As Lipschitz condition is not enforced by our method, we do not derive a theoretical proof for convergence, but empirically demonstrate that it always converges, and usually in 3 to 6 iterations. At most 7 iterations were needed for maximum inversion error less than 10^{-2} voxels for the whole volume (Appendix V). The good convergence follows from limiting individual deformations predicted by $u^{(k)}$ to be small by hard constraint which also ensures topology preservation, see details in Appendix I. Also, as demonstrated by the main experiments, our method produces topology preserving deformations almost everywhere.

3.4 Training and implementation

We train the model in an unsupervised end-to-end manner similarly to most other unsupervised registration methods, by using similarity and deformation regularization losses. The similarity loss encourages deformed images to be similar to the target images, and the regularity loss encourages desirable properties, such as smoothness, on the predicted deformations. For similarity we use local normalized cross-correlation with window width 7 and for regularization we use L^2 gradient penalty on the displacement fields, identically to VoxelMorph (Balakrishnan et al., 2019). We apply the losses in both directions to maintain symmetry. One could apply the losses in the intermediate coordinates and avoid building the full deformations during training. However, we do not do this since we expect that applying the losses in the original image coordinates yields the best results. The final loss is:

$$\mathcal{L} = \text{NCC}(x_1 \circ \phi, x_2) + \text{NCC}(x_2 \circ \phi^{-1}, x_1) + \lambda * [\text{Grad}(d(\phi)) + \text{Grad}(d(\phi^{-1}))], \quad (9)$$

where ϕ is a deformation, $d(\cdot)$ the displacement field, NCC the local normalized cross-correlation loss, and Grad the gradient loss. For details on hyperparameter selection, see Appendix II. Our implementation is in PyTorch (Paszke et al., 2019), and can be found at <https://github.com/honkanj/SITReg>. Evaluation methods and preprocessing done by us, see Section 4, are included.

4 Experimental setup

Datasets: We use two subject-to-subject registration datasets: *OASIS* brains dataset with 414 T1-weighted brain MRI images (Marcus et al., 2007) as pre-processed for Learn2Reg challenge (Hoopes et al., 2021; Hering et al., 2022) (data use agreement website ¹), and *LPBA40* dataset from University of California Laboratory of Neuro Imaging (USC LONI) with 40 brain MRI images (Shattuck et al., 2008) (LONI Research License, Version 3.0²). Pre-processing for both datasets includes bias field correction, normalization, and cropping. For OASIS dataset we use affinely pre-aligned images and for LPBA40 dataset we use rigidly pre-aligned images. Additionally we train our model without any pre-alignment on OASIS data (*OASIS raw*) to test our method with larger initial displacements. Voxel sizes of the affinely aligned and raw datasets are the same but volume sizes differ. Details of the split into training, validation, and test sets, and cropping and resolution can be found in Appendix VIII.

¹<https://www.oasis-brains.org/#access>

²<https://resource.loni.usc.edu/resources/atlas/licenses-agreement/>

Table 1: **Results for the OASIS dataset.** Mean and standard deviation of each metric are computed on the test set. VoxelMorph and cLapIRN do not predict inverse deformations and hence the inverse-consistency error is not shown. Determinant standard deviation and the consistency metrics are omitted for the SITReg trained with the non-affinely-aligned raw data since they are not comparable with other results (the omitted values were 0.18(0.028), 1.2e-3(2.7e-4), and 1.2e-3(2.7e-4)).

Model	Accuracy		Deformation regularity		Consistency	
	Dice \uparrow	HD95 \downarrow	$ J_\phi \leq 0 \downarrow$	$\text{std}(J_\phi) \downarrow$	Cycle \downarrow	Inverse \downarrow
SYMNet (original)	0.788(0.029)	2.15(0.57)	0.32 (0.98)	0.42 (0.038)	3.0e-1(2.9e-2)	3.5e-3 (4.2e-4)
SYMNet (no anti-fold)	0.787(0.029)	2.17(0.58)	86(37)	0.44(0.043)	2.8e-1(2.8e-2)	5.2e-3(8.4e-4)
VoxelMorph	0.803(0.031)	2.08(0.57)	3.4e3(2.3e3)	0.46(0.030)	4.5e-1(5.3e-2)	-
cLapIRN	0.812(0.027)	1.93(0.50)	3.8e4(7.7e3)	0.52(0.030)	1.2e0(1.6e-1)	-
SITReg	0.817 (0.025)*	1.85(0.46)*	11(5.6)	0.42 (0.035)	5.6e-3 (6.9e-4)*	5.6e-3(6.9e-4)
SITReg (raw data)	0.810(0.024)	1.81 (0.54)*	1.5(1.9)	-	-	-

* Statistically significant ($p < 0.05$) improvement compared to the baselines, for details see Appendix IX.

Evaluation metrics: We evaluate the *registration accuracy* using segmentations included in the datasets: automatic segmentations of 35 brain structures for OASIS and manual segmentations of 56 brain structures for LPBA40. We use two metrics: Dice score (Dice) and 95% quantile of the Hausdorff distances (HD95) between the segmentations of each structure, similarly to Learn2Reg challenge (Hering et al., 2022). Dice score measures overlap of the segmentations and Hausdorff distance measures the distance between the surfaces of the segmentations. We compare the segmentations of the source images deformed by the method and the segmentations of the target images. However, evaluating registration methods solely based on overlap of anatomic regions has its limitations (Pluim et al., 2016; Rohlfing, 2011), and hence also *deformation regularity* should be measured. As is common, we evaluate the regularity of the generated deformations by metrics based on the local Jacobian determinant. We measure topology preservation by counting the number voxels with negative determinant ($|J_\phi| \leq 0$), and smoothness by computing the standard deviation of the determinant ($\text{std}(|J_\phi|)$). A negative determinant means the deformation is not topology preserving at that location. Additionally, we measure inverse and cycle *consistency* errors, introduced in Section 1.

Baselines: We compare against *VoxelMorph* (Balakrishnan et al., 2019), *SYMNet* (Mok and Chung, 2020a), and conditional LapIRN (*cLapIRN*) (Mok and Chung, 2020b, 2021). VoxelMorph is a standard baseline in deep learning based unsupervised registration. With SYMNet we are interested in how well our method preserves topology and how accurate the generated inverse deformations are compared to SVF based methods. Additionally, since SYMNet is symmetric from the loss point of view, it is interesting to see how symmetric predictions it produces in practice. cLapIRN was the best method on OASIS dataset in Learn2Reg 2021 challenge (Hering et al., 2022). We used the official implementations³⁴⁵ adjusted to our datasets. SYMNet uses anti-folding loss to penalize negative determinant. Since this loss is a separate component that could be easily used with any method, we also train SYMNet without it (*SYMNet, no anti-fold*). This provides a comparison on how well the vanilla SVF framework can generate invertible deformations in comparison to our method. For details on hyperparameter selection for baseline models, see Appendix III.

5 Results

The results for the OASIS dataset are in Table 1 and for LPBA40 in Table 2. Tissue overlap results on individual anatomical regions can be found in Appendix VII. The proposed method performs very well on both datasets in terms of registration accuracy: dice score and HD95 are equal to or better than for any baseline. In addition, the generated deformations have very little folding, similar to the diffeomorphic SVF-based SYMNet, which justifies calling our algorithm topology preserving. The number of folding voxels for both our method and SYMNet is extremely small, only a few in the whole volume of millions of voxels, whereas cLapIRN and VoxelMorph have significantly more folding voxels. In terms of cycle consistency, our method outperforms all the baseline models by

³<https://github.com/voxelmorph/voxelmorph>

⁴<https://github.com/cwmok/Fast-Symmetric-Diffeomorphic-Image-Registration-with-Convolutional-Neural-Networks>

⁵https://github.com/cwmok/Conditional_LapIRN/

Table 2: **Results for the LPBA40 experiment.** Mean and standard deviation of each metric are computed on the test set. VoxelMorph and cLapIRN do not predict inverse deformations and hence the inverse-consistency error is not shown.

Model	Accuracy		Deformation regularity		Consistency	
	Dice \uparrow	HD95 \downarrow	$ J_\phi _{\leq 0} \downarrow$	$\text{std}(J_\phi) \downarrow$	Cycle \downarrow	Inverse \downarrow
SYMNet (original)	0.669(0.033)	6.79(0.70)	0.69 (2.2)	0.34(0.049)	2.7e-1(6.1e-2)	2.1e-3 (4.3e-4)
SYMNet (no anti-fold)	0.664(0.034)	6.88(0.73)	14.(10.)	0.36(0.052)	2.8e-1(5.8e-2)	2.9e-3(6.7e-4)
VoxelMorph	0.676(0.032)	6.72(0.68)	7.2e3(8.4e3)	0.34(0.035)	3.1e-1(1.1e-1)	-
cLapIRN	0.714(0.019)	5.93(0.43)	3.0e3(1.1e3)	0.26 (0.019)	5.6e-1(1.8e-1)	-
SITReg	0.716 (0.017)	5.91 (0.41)	1.8(2.1)	0.29(0.029)	2.7e-3 (4.1e-4)*	2.7e-3(4.1e-4)

* Statistically significant ($p < 0.05$) improvement compared to the baselines, for details see Appendix IX.

Table 3: **Computational efficiency on the OASIS dataset.** Mean and standard deviation values are shown. Inference time and inference memory usage were measured on NVIDIA GeForce RTX 3090. The images raw dataset without pre-alignment have 3.8 times more voxels resulting in significantly larger inference time and memory usage for the SITReg model trained with it.

Model	Inference Time (s) \downarrow	Inference Memory (GB) \downarrow	# parameters (M) \downarrow
SYMNet (original)	0.10 (0.0010)	1.6	0.9
SYMNet (simple)	0.10 (0.0011)	1.6	0.9
VoxelMorph	0.17 (0.00078)	5.4	1.3
cLapIRN	0.11 (0.00085)	4.1	1.2
SITReg	0.47 (0.032)	2.9	1.2
SITReg (raw data)	2.0 (0.022)	11.1	2.5

a significant margin, and in terms of inverse consistency our method is similar to the SVF based SYMNet, which performs very well, showcasing that our method is indeed inverse consistent by construct. Interestingly, the model trained with non-affinely-aligned OASIS data performs equally well to the model trained with affinely aligned data, which demonstrates that the method is capable of accurately registering images even with large initial misalignments.

The assessment of registration performance should not be based on a single metric, e.g., segmentation based metrics, but instead on the overall performance with respect to different metrics, similarly to, e.g., the Learn2reg challenge (Hering et al., 2022). In the overall comparison, our method has better registration performance than the baselines since no baseline clearly outperforms our method on any metric, but our method outperforms each baseline clearly on at least two metrics: While cLapIRN performs similarly to our method in terms of tissue overlap metrics, our method achieves that with far fewer folding voxels and better cycle consistency, and while SYMNet performs similarly or slightly better in terms of deformation regularity and inverse consistency, our method performs significantly better on tissue overlap and cycle consistency metrics.

A comparison of the methods’ efficiencies is in Table 3. Inference time of our method is slightly larger than that of the compared methods, but unlike VoxelMorph and cLapIRN, it produces deformations in both directions immediately. Also, half a second runtime is still very fast and restrictive only in the most time-critical use cases. In terms of memory usage our method is very competitive.

6 Conclusions

We proposed a novel image registration architecture inbuilt with the desirable inductive biases of symmetry, inverse consistency, and topology preservation. The multi-resolution formulation was capable of accurately registering images even with large initial misalignments. As part of our method, we developed a new neural network component *deformation inversion layer*. The model is easily end-to-end trainable and does not require tedious multi-stage training strategies. In the experiments the method demonstrated state-of-the-art registration performance. The main limitations are the somewhat heavier computational cost than other methods, and the lack of theoretical convergence guarantees, especially for larger deformations, although in practice good performance was observed.

Acknowledgments and Disclosure of Funding

This work was supported by the Academy of Finland (Flagship programme: Finnish Center for Artificial Intelligence FCAI, and grants 336033, 352986) and EU (H2020 grant 101016775 and NextGenerationEU).

Data were provided in part by OASIS-1: Cross-Sectional: Principal Investigators: D. Marcus, R. Buckner, J. Csernansky J. Morris; P50 AG05681, P01 AG03991, P01 AG026276, R01 AG021910, P20 MH071616, U24 RR021382.

We also acknowledge the computational resources provided by the Aalto Science-IT Project.

References

V. Arsigny, O. Commowick, X. Pennec, and N. Ayache. A log-euclidean framework for statistics on diffeomorphisms. In *International Conference on Medical Image Computing and Computer-Assisted Intervention*, pages 924–931. Springer, 2006.

J. Ashburner. A fast diffeomorphic image registration algorithm. *Neuroimage*, 38(1):95–113, 2007.

B. B. Avants, C. L. Epstein, M. Grossman, and J. C. Gee. Symmetric diffeomorphic image registration with cross-correlation: evaluating automated labeling of elderly and neurodegenerative brain. *Medical image analysis*, 12(1):26–41, 2008.

S. Bai, J. Z. Kolter, and V. Koltun. Deep equilibrium models. *Advances in Neural Information Processing Systems*, 32, 2019.

S. Bai, V. Koltun, and J. Z. Kolter. Multiscale deep equilibrium models. *Advances in Neural Information Processing Systems*, 33:5238–5250, 2020.

G. Balakrishnan, A. Zhao, M. R. Sabuncu, J. Guttag, and A. V. Dalca. VoxelMorph: A learning framework for deformable medical image registration. *IEEE transactions on medical imaging*, 38(8):1788–1800, 2019.

Y. Cao, M. I. Miller, R. L. Winslow, and L. Younes. Large deformation diffeomorphic metric mapping of vector fields. *IEEE transactions on medical imaging*, 24(9):1216–1230, 2005.

M. Chen, W. Lu, Q. Chen, K. J. Ruchala, and G. H. Olivera. A simple fixed-point approach to invert a deformation field. *Medical physics*, 35(1):81–88, 2008.

Y. Choi and S. Lee. Injectivity conditions of 2D and 3D uniform cubic B-spline functions. *Graphical models*, 62(6):411–427, 2000.

G. E. Christensen, R. D. Rabbitt, M. I. Miller, S. C. Joshi, U. Grenander, T. A. Coogan, and D. C. Van Essen. Topological properties of smooth anatomic maps. In *Information processing in medical imaging*, volume 3, page 101. Springer Science & Business Media, 1995.

A. V. Dalca, G. Balakrishnan, J. Guttag, and M. R. Sabuncu. Unsupervised learning for fast probabilistic diffeomorphic registration. In *Medical Image Computing and Computer Assisted Intervention–MICCAI 2018: 21st International Conference, Granada, Spain, September 16–20, 2018, Proceedings, Part I*, pages 729–738. Springer, 2018.

D. Duvenaud, J. Z. Kolter, and M. Johnson. Deep implicit layers tutorial-neural ODEs, deep equilibrium models, and beyond. *Neural Information Processing Systems Tutorial*, 2020.

T. Estienne, M. Vakalopoulou, E. Battistella, T. Henry, M. Lerousseau, A. Leroy, N. Paragios, and E. Deutsch. MICS: Multi-steps, inverse consistency and symmetric deep learning registration network. *arXiv preprint arXiv:2111.12123*, 2021.

D. Gu, X. Cao, S. Ma, L. Chen, G. Liu, D. Shen, and Z. Xue. Pair-wise and group-wise deformation consistency in deep registration network. In *International Conference on Medical Image Computing and Computer-Assisted Intervention*, pages 171–180. Springer, 2020.

K. He, X. Zhang, S. Ren, and J. Sun. Deep residual learning for image recognition. In *Proceedings of the IEEE conference on computer vision and pattern recognition*, pages 770–778, 2016.

A. Hering, L. Hansen, T. C. Mok, A. C. Chung, H. Siebert, S. Häger, A. Lange, S. Kuckertz, S. Heldmann, W. Shao, et al. Learn2Reg: Comprehensive multi-task medical image registration challenge, dataset and evaluation in the era of deep learning. *IEEE Transactions on Medical Imaging*, 2022.

A. Hoopes, M. Hoffmann, B. Fischl, J. Guttag, and A. V. Dalca. Hypermorph: Amortized hyperparameter learning for image registration. In *International Conference on Information Processing in Medical Imaging*, pages 3–17. Springer, 2021.

J. E. Iglesias. A ready-to-use machine learning tool for symmetric multi-modality registration of brain mri. *Scientific Reports*, 13(1):6657, 2023.

B. Kim, J. Kim, J.-G. Lee, D. H. Kim, S. H. Park, and J. C. Ye. Unsupervised deformable image registration using cycle-consistent CNN. In *International Conference on Medical Image Computing and Computer-Assisted Intervention*, pages 166–174. Springer, 2019.

A. Klein, J. Andersson, B. A. Ardekani, J. Ashburner, B. Avants, M.-C. Chiang, G. E. Christensen, D. L. Collins, J. Gee, P. Hellier, et al. Evaluation of 14 nonlinear deformation algorithms applied to human brain mri registration. *Neuroimage*, 46(3):786–802, 2009.

J. Krebs, T. Mansi, B. Mailhé, N. Ayache, and H. Delingette. Unsupervised probabilistic deformation modeling for robust diffeomorphic registration. In *Deep Learning in Medical Image Analysis and Multimodal Learning for Clinical Decision Support*, pages 101–109. Springer, 2018.

J. Krebs, H. Delingette, B. Mailhé, N. Ayache, and T. Mansi. Learning a probabilistic model for diffeomorphic registration. *IEEE transactions on medical imaging*, 38(9):2165–2176, 2019.

D. Mahapatra and Z. Ge. Training data independent image registration with GANs using transfer learning and segmentation information. In *2019 IEEE 16th International Symposium on Biomedical Imaging (ISBI 2019)*, pages 709–713. IEEE, 2019.

D. S. Marcus, T. H. Wang, J. Parker, J. G. Csernansky, J. C. Morris, and R. L. Buckner. Open Access Series of Imaging Studies (OASIS): Cross-sectional MRI data in young, middle aged, nondemented, and demented older adults. *Journal of cognitive neuroscience*, 19(9):1498–1507, 2007.

T. C. Mok and A. Chung. Fast symmetric diffeomorphic image registration with convolutional neural networks. In *Proceedings of the IEEE/CVF conference on computer vision and pattern recognition*, pages 4644–4653, 2020a.

T. C. Mok and A. Chung. Large deformation diffeomorphic image registration with laplacian pyramid networks. In *International Conference on Medical Image Computing and Computer-Assisted Intervention*, pages 211–221. Springer, 2020b.

T. C. Mok and A. Chung. Conditional deformable image registration with convolutional neural network. In *International Conference on Medical Image Computing and Computer-Assisted Intervention*, pages 35–45. Springer, 2021.

M. Niethammer, R. Kwitt, and F.-X. Vialard. Metric learning for image registration. In *Proceedings of the IEEE/CVF Conference on Computer Vision and Pattern Recognition*, pages 8463–8472, 2019.

F. P. Oliveira and J. M. R. Tavares. Medical image registration: a review. *Computer methods in biomechanics and biomedical engineering*, 17(2):73–93, 2014.

A. Paszke, S. Gross, F. Massa, A. Lerer, J. Bradbury, G. Chanan, T. Killeen, Z. Lin, N. Gimelshein, L. Antiga, A. Desmaison, A. Kopf, E. Yang, Z. DeVito, M. Raison, A. Tejani, S. Chilamkurthy, B. Steiner, L. Fang, J. Bai, and S. Chintala. Pytorch: An imperative style, high-performance deep learning library. In *Advances in Neural Information Processing Systems 32*, pages 8024–8035. Curran Associates, Inc., 2019. URL <http://papers.neurips.cc/paper/9015-pytorch-an-imperative-style-high-performance-deep-learning-library.pdf>.

J. P. Pluim, S. E. Muenzing, K. A. Eppenhof, and K. Murphy. The truth is hard to make: Validation of medical image registration. In *2016 23rd International Conference on Pattern Recognition (ICPR)*, pages 2294–2300. IEEE, 2016.

T. Rohlfing. Image similarity and tissue overlaps as surrogates for image registration accuracy: widely used but unreliable. *IEEE transactions on medical imaging*, 31(2):153–163, 2011.

D. Rueckert, L. I. Sonoda, C. Hayes, D. L. Hill, M. O. Leach, and D. J. Hawkes. Nonrigid registration using free-form deformations: Application to breast MR images. *IEEE Transactions on Medical Imaging*, 18(8):712–721, 1999.

D. Rueckert, P. Aljabar, R. A. Heckemann, J. V. Hajnal, and A. Hammers. Diffeomorphic registration using B-splines. In *International Conference on Medical Image Computing and Computer-Assisted Intervention*, pages 702–709. Springer, 2006.

D. W. Shattuck, M. Mirza, V. Adisetiyo, C. Hojatkashani, G. Salamon, K. L. Narr, R. A. Poldrack, R. M. Bilder, and A. W. Toga. Construction of a 3D probabilistic atlas of human cortical structures. *Neuroimage*, 39(3):1064–1080, 2008.

Z. Shen, X. Han, Z. Xu, and M. Niethammer. Networks for joint affine and non-parametric image registration. In *Proceedings of the IEEE/CVF Conference on Computer Vision and Pattern Recognition*, pages 4224–4233, 2019a.

Z. Shen, F.-X. Vialard, and M. Niethammer. Region-specific diffeomorphic metric mapping. *Advances in Neural Information Processing Systems*, 32, 2019b.

A. Sotiras, C. Davatzikos, and N. Paragios. Deformable medical image registration: A survey. *IEEE transactions on medical imaging*, 32(7):1153–1190, 2013.

H. F. Walker and P. Ni. Anderson acceleration for fixed-point iterations. *SIAM Journal on Numerical Analysis*, 49(4):1715–1735, 2011.

S. I. Young, Y. Balbastre, A. V. Dalca, W. M. Wells, J. E. Iglesias, and B. Fischl. SuperWarp: Supervised learning and warping on U-Net for invariant subvoxel-precise registration. *arXiv preprint arXiv:2205.07399*, 2022.

J. Zhang. Inverse-consistent deep networks for unsupervised deformable image registration. *arXiv preprint arXiv:1809.03443*, 2018.

Y. Zheng, X. Sui, Y. Jiang, T. Che, S. Zhang, J. Yang, and H. Li. Symreg-gan: symmetric image registration with generative adversarial networks. *IEEE transactions on pattern analysis and machine intelligence*, 44(9):5631–5646, 2021.

Appendices

SITReg: Multi-resolution architecture for symmetric, inverse consistent, and topology preserving image registration using deformation inversion layers

Joel Honkamaa

Department of Computer Science
Aalto University
Aalto, Finland
joel.honkamaa@aalto.fi

Pekka Marttinen

Department of Computer Science
Aalto University
Aalto, Finland
pekka.marttinen@aalto.fi

I Architectural details

The neural networks $u^{(k)}$ used for predicting deformations (in Equation 5) consist of the following components (in order):

1. Concatenation of the two inputs along the channel dimension. Before concatenation we reparametrize the features as subtraction of the inputs and the sum of the inputs as suggested by Young et al. (2022).
2. Two convolutions with some non-linear activation after each of the convolutions.
3. Convolution with kernel of spatial size 1
4. $\gamma \times \text{Tanh}$ function where the $\gamma \in \mathbb{R}^+$ is a scaling factor defining maximum displacement. We used the value $\gamma = 0.15$ (voxels) in the experiments. The voxel size is voxel size of each resolution (lower resolution levels have larger voxels).
5. Upsampling with prefiltered cubic spline interpolation (Ruijters and Thévenaz, 2012) to the full resolution. Spline interpolation can be implemented efficiently using transposed convolutions (De Vos et al., 2019). The deformation is upsampled since it needs to be inverted and otherwise the generated inverse would not be accurate in the full resolution.

We equate the resulting displacement field with the deformation. Limiting the range of values with the scaled Tanh activation is important since by that we ensure that individual predicted deformation are invertible, which in turn ensures topology preservation and convergence of the fixed point iteration. The chosen constraint was concluded to provide enough freedom while resulting in almost everywhere invertible final deformations (the performance is similar to the SVF (Arsigny et al., 2006) based methods). We also experimented with value $\gamma = 0.3$ which also performed well but chose the $\gamma = 0.15$ for the final experiments. More details on this can be found in Appendix II. Note that since the displacements are in the voxel size of each resolution level, the displacements at lower resolutions correspond to larger displacements at the full resolution (scaling is performed during the upsampling).

II Hyperparameter selection details

We experimented on validation set with different hyperparameters during the development. While the final results on test set are computed only for one chosen configuration, the results on validation set might still be of interest for the reader. Results of these experiments for the OASIS dataset are shown in Table A1 and for the LPBA40 dataset in Table A2.

Table A1: Hyperparameter optimization results for our method calculated on the OASIS validation set. The chosen configuration was $\lambda = 1.0$, $\gamma = 0.15$, and $K = 5$. HD95 metric is not included due to relatively high computational cost. Here γ corresponds to the scaling factor described in Appendix I

Hyperparameters			Accuracy		Deformation regularity		Consistency	
λ	γ	K	Dice \uparrow	$ J_\phi \leq 0 \downarrow$	$\text{std}(J_\phi) \downarrow$	Cycle \downarrow	Inverse \downarrow	
1.0	0.15	5	0.820(0.034)	11.(5.5)	0.42(0.025)	5.5e-3(5.8e-4)	5.5e-3(5.8e-4)	
1.5	0.15	5	0.817(0.035)	0.43(0.84)	0.38(0.022)	3.5e-3(3.3e-4)	3.5e-3(3.3e-4)	
2.0	0.15	5	0.814(0.035)	0.0053(0.072)	0.35(0.020)	2.4e-3(2.2e-4)	2.4e-3(2.2e-4)	
1.0	0.3	4	0.823(0.034)	66.(19.)	0.43(0.026)	8.0e-3(8.2e-4)	8.0e-3(8.2e-4)	
1.5	0.3	4	0.819(0.035)	5.1(3.6)	0.39(0.022)	4.9e-3(4.8e-4)	4.9e-3(4.8e-4)	
2.0	0.3	4	0.815(0.035)	0.42(0.91)	0.36(0.020)	3.6e-3(3.1e-4)	3.6e-3(3.1e-4)	

Table A2: Hyperparameter optimization results for our method calculated on the LPBA40 validation set. The chosen configuration was $\lambda = 1.0$, $\gamma = 0.15$, $K = 7$, and Affine = No. Here γ corresponds to the scaling factor described in Appendix I

Hyperparameters				Accuracy		Deformation regularity		Consistency	
λ	γ	K	Affine	Dice \uparrow	HD95 \downarrow	$ J_\phi \leq 0 \downarrow$	$\text{std}(J_\phi) \downarrow$	Cycle \downarrow	Inverse \downarrow
1.0	0.15	5	No	0.710(0.016)	6.03(0.42)	1.8(1.9)	0.28(0.018)	2.7e-3(3.4e-4)	2.7e-3(3.4e-4)
1.0	0.15	6	No	0.717(0.014)	5.82(0.35)	0.80(1.1)	0.28(0.017)	2.6e-3(3.0e-4)	2.6e-3(3.0e-4)
1.0	0.15	7	No	0.719(0.013)	5.80(0.32)	1.4(1.8)	0.27(0.017)	2.4e-3(3.0e-4)	2.4e-3(3.0e-4)
1.0	0.15	5	Yes	0.711(0.017)	5.99(0.45)	1.4(1.3)	0.28(0.018)	2.5e-3(3.2e-4)	2.5e-3(3.2e-4)
1.0	0.15	6	Yes	0.718(0.013)	5.79(0.31)	1.4(1.4)	0.28(0.017)	2.5e-3(3.2e-4)	2.5e-3(3.2e-4)
1.0	0.3	4	No	0.706(0.014)	6.09(0.38)	14.(5.0)	0.29(0.019)	3.2e-3(4.8e-4)	3.2e-3(4.8e-4)
1.0	0.3	5	No	0.718(0.013)	5.87(0.36)	11.(5.3)	0.29(0.019)	3.5e-3(4.6e-4)	3.5e-3(4.6e-4)
1.0	0.3	6	No	0.721(0.014)	5.74(0.33)	10.(6.1)	0.29(0.018)	3.5e-3(4.6e-4)	3.5e-3(4.6e-4)

For the OASIS dataset we experimented with two configurations of number of resolution levels K and maximum displacements γ . With both of these configurations we tested three different values for the regularization weight λ .

For the LPBA40 dataset we experimented with 8 configurations of number of resolution levels K , maximum displacements γ , and whether to predict an affine transformation, but used the regularization weight value $\lambda = 1.0$ for all of them.

Smaller maximum displacement was chosen for both of the experiments since the resulting deformations had better properties with only small decrease in accuracy.

With the raw OASIS dataset without pre-alignment we used 6 resolution levels, together with an affine transformation prediction stage before the other deformation updates. We omitted the predicted affine transformation from the deformation regularization.

III Hyperparameter selection details for baselines

For cLapIRN baseline we used the regularization parameter value $\bar{\lambda} = 0.05$ for the OASIS dataset and value $\bar{\lambda} = 0.1$ for the LPBA40 dataset where $\bar{\lambda}$ is used as in the paper presenting the method (Mok and Chung, 2021). The values were chosen based on the validation set results shown in Tables A3 and A4.

We trained VoxelMorph with losses and regularization weight identical to our method and for SYMNet we used hyperparameters directly provided by Mok and Chung (2020a). We used the default number of convolution features for the baselines except for VoxelMorph we doubled the number of features, as suggested for subject-to-subject registration by Balakrishnan et al. (2019).

Table A3: Regularization parameter optimization results for cLapIRN calculated on the OASIS validation set. Here $\bar{\lambda}$ refers to the normalized regularization weight of the gradient loss of cLapIRN and should be in range $[0, 1]$. Value $\bar{\lambda} = 0.05$ was chosen since it resulted in clearly the highest Dice score. HD95 metric is not included due to relatively high computational cost.

Hyperparameters	Accuracy		Deformation regularity		Consistency
	$\bar{\lambda}$	Dice \uparrow	$ J_\phi _{\leq 0} \downarrow$	$\text{std}(J_\phi) \downarrow$	
0.01	0.812(0.034)	9.2e4(1.1e4)	0.75(0.040)	1.7e0(1.5e-1)	
0.05	0.817(0.034)	3.8e4(6.7e3)	0.53(0.026)	1.2e0(1.3e-1)	
0.1	0.812(0.035)	1.5e4(4.0e3)	0.41(0.019)	8.9e-1(1.1e-1)	
0.2	0.798(0.038)	2.3e3(1.3e3)	0.30(0.013)	6.0e-1(8.3e-2)	
0.4	0.769(0.042)	2.2e1(3.4e1)	0.18(0.0088)	3.5e-1(4.4e-2)	
0.8	0.727(0.049)	1.6e-2(2.2e-1)	0.10(0.0051)	2.5e-1(3.8e-2)	
1.0	0.711(0.052)	0.0e0.0(0.0e0.0)	0.081(0.0043)	2.3e-1(3.8e-2)	

Table A4: Regularization parameter optimization results for cLapIRN calculated on the LPBA40 validation set. Here $\bar{\lambda}$ refers to the normalized regularization weight of the gradient loss of cLapIRN and should be in range $[0, 1]$. Value $\bar{\lambda} = 0.1$ was chosen due to the best overall performance.

Hyperparameters	Accuracy		Deformation regularity		Consistency
	$\bar{\lambda}$	Dice \uparrow	HD95 \downarrow	$ J_\phi _{\leq 0} \downarrow$	
0.01	0.714(0.014)	5.86(0.35)	3.7e4(5.8e3)	0.43(0.017)	9.9e-1(2.2e-1)
0.05	0.715(0.014)	5.87(0.35)	1.2e4(2.6e3)	0.32(0.013)	8.0e-1(2.1e-1)
0.1	0.714(0.014)	5.88(0.36)	2.6e3(8.7e2)	0.25(0.010)	6.6e-1(2.1e-1)
0.2	0.709(0.015)	5.92(0.38)	1.3e2(7.4e1)	0.18(0.0085)	4.9e-1(1.9e-1)
0.4	0.698(0.017)	6.03(0.42)	5.0e-2(2.2e-1)	0.13(0.0070)	3.6e-1(1.9e-1)
0.8	0.678(0.019)	6.23(0.48)	0.0e0.0(0.0e0.0)	0.085(0.0062)	3.0e-1(1.9e-1)
1.0	0.671(0.021)	6.31(0.51)	0.0e0.0(0.0e0.0)	0.073(0.0061)	3.0e-1(1.9e-1)

IV Proof of Proposition 3.1

IV.A Inverse consistent by construct

Proof. Inverse consistency by construct follows directly from Equation 8:

$$\begin{aligned}
 f_{1 \rightarrow 2}(x_1, x_2) &= f_{1 \rightarrow 1.5}^{(0)}(x_1, x_2) \circ f_{2 \rightarrow 1.5}^{(0)}(x_1, x_2)^{-1} \\
 &= \left(f_{2 \rightarrow 1.5}^{(0)}(x_1, x_2) \circ f_{1 \rightarrow 1.5}^{(0)}(x_1, x_2)^{-1} \right)^{-1} \\
 &= f_{2 \rightarrow 1}(x_1, x_2)^{-1}
 \end{aligned}$$

□

As discussed in Section 1, inverse consistency error is not exactly zero even for earlier methods guaranteeing inverse consistency by construct, and the same is true here. Here the remaining error can be in principle from three sources: limited spatial sampling resolution, deformation inversion layer not converging, or lack of invertibility of deformations. However, as shown in Appendix V, the error caused by fixed point iteration not converging is tiny. Lack of invertibility should also not be a large source of error since as shown by the main experiments, the deformations are almost everywhere invertible. Hence the remaining inverse consistency error should be mostly caused by limited spatial sampling resolution, conclusion supported by the main experiments, where error of similar magnitude to that of diffeomorphic SVF framework was obtained.

IV.B Symmetric by construct

Proof. We use induction. Assume that for any x_1 and x_2 at level $k + 1$ the following holds: $f_{1 \rightarrow 1.5}^{(k+1)}(x_1, x_2) = f_{2 \rightarrow 1.5}^{(k+1)}(x_2, x_1)$. For level K it holds trivially since $f_{1 \rightarrow 1.5}^{(K)}(x_1, x_2)$ and $f_{2 \rightarrow 1.5}^{(K)}(x_1, x_2)$ are defined as identity deformations. For the proof we view $z_1^{(k)}$, $z_2^{(k)}$, and $U^{(k)}$ as functions of the input images, although not explicitly marked in the main paper. Using the induction assumption we have at level k :

$$z_1^{(k)}(x_1, x_2) = h^{(k)}(x_1) \circ f_{1 \rightarrow 1.5}^{(K)}(x_1, x_2) = h^{(k)}(x_1) \circ f_{2 \rightarrow 1.5}^{(K)}(x_2, x_1) = z_2^{(k)}(x_2, x_1)$$

Then also:

$$\begin{aligned}
U^{(k)}(x_1, x_2) &= u^{(k)}(z_1^{(k)}(x_1, x_2), z_2^{(k)}(x_1, x_2)) \circ u^{(k)}(z_2^{(k)}(x_1, x_2), z_1^{(k)}(x_1, x_2))^{-1} \\
&= u^{(k)}(z_2^{(k)}(x_2, x_1), z_1^{(k)}(x_2, x_1)) \circ u^{(k)}(z_1^{(k)}(x_2, x_1), z_2^{(k)}(x_2, x_1))^{-1} \\
&= \left[u^{(k)}(z_1^{(k)}(x_2, x_1), z_2^{(k)}(x_2, x_1)) \circ u^{(k)}(z_2^{(k)}(x_2, x_1), z_1^{(k)}(x_2, x_1))^{-1} \right]^{-1} \\
&= U^{(k)}(x_2, x_1)^{-1}
\end{aligned}$$

Then we can finalize the induction step:

$$\begin{aligned}
f_{1 \rightarrow 1.5}^{(k)}(x_1, x_2) &= f_{1 \rightarrow 1.5}^{(k+1)}(x_1, x_2) \circ U^{(k)}(x_1, x_2) \\
&= f_{2 \rightarrow 1.5}^{(k+1)}(x_2, x_1) \circ U^{(k)}(x_2, x_1)^{-1} = f_{2 \rightarrow 1.5}^{(k)}(x_2, x_1)
\end{aligned}$$

From this follows that the method is symmetric by construct:

$$\begin{aligned}
f_{1 \rightarrow 2}(x_1, x_2) &= f_{1 \rightarrow 1.5}^{(0)}(x_1, x_2) \circ f_{2 \rightarrow 1.5}^{(0)}(x_1, x_2)^{-1} \\
&= f_{2 \rightarrow 1.5}^{(0)}(x_2, x_1) \circ f_{1 \rightarrow 1.5}^{(0)}(x_2, x_1)^{-1} = f_{2 \rightarrow 1}(x_2, x_1)
\end{aligned}$$

Unlike inverse consistency by construct, this relation holds exactly. \square

V Fixed point iteration convergence in deformation inversion layers

We conducted an experiment on the fixed point iteration convergence in the deformation inversion layers with the model trained on OASIS dataset. The results can be seen in Figure A1. The main result was that in the whole OASIS test set of 9591 pairs not a single deformation required more than 7 iterations for convergence. Deformations requiring 7 iterations were only 0.13% of all the deformations and a significant majority of the deformations (96%) required 3 to 5 iterations. In all the experiments, including this one, the stopping criterion for the iterations was maximum displacement error within the whole volume reaching below one hundredth of a voxel, which is a very small error. In conclusion, lack of convergence of the fixed point iteration in the deformation inversion layer does not introduce practically relevant error.

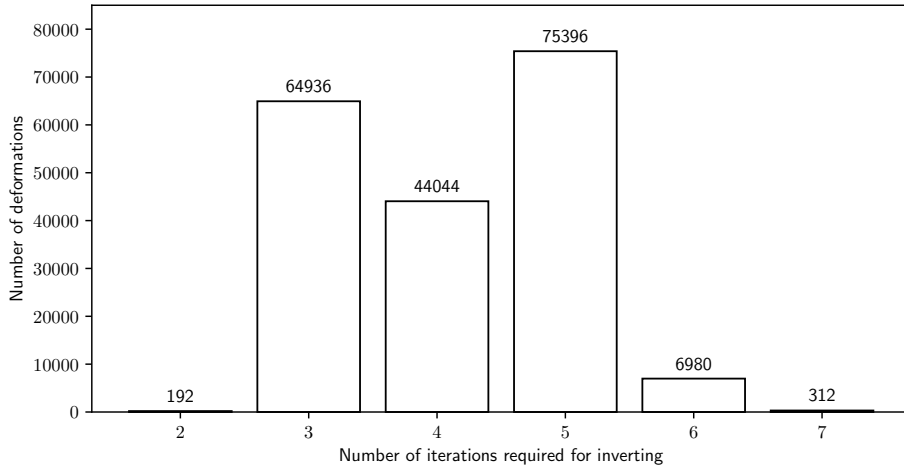


Figure A1: Number of fixed point iterations required for convergence in deformation inversion layers with the model trained on OASIS dataset. The stopping criterion for the fixed point iteration was maximum displacement error within the whole volume reaching below one hundredth of a voxel. All deformation inversions for the whole OASIS test set are included.

VI Deformation inversion layer memory usage

We conducted an experiment on the memory usage of the deformation inversion layer compared to the stationary velocity field (SVF) framework (Arsigny et al., 2006) since SVF framework could also be used to implement the suggested architecture in practice.

With the SVF framework one could slightly simplify the deformation update Equation 5 to the form

$$U^{(k)} := \exp(u^{(k)}(z_1^{(k)}, z_2^{(k)}) - u^{(k)}(z_2^{(k)}, z_1^{(k)})) \quad (\text{A1})$$

where \exp is the SVF integration (corresponding to Lie algebra exponentiation), and $u^{(k)}$ now predicts an auxiliary velocity field. We compared memory usage of this to our implementation, and used the implementation by Dalca et al. (2018) for SVF integration.

The results are shown in Table A5. Our version implemented using the deformation inversion layer requires 5 times less data to be stored in memory for the backward pass compared to the SVF integration. The peak memory usage during the inversion is also slightly lower. The memory saving is due to the memory efficient back-propagation through the fixed point iteration layers, which requires only the final inverted volume to be stored for backward pass. Since our architecture requires two such operations for each resolution level ($U^{(k)}$ and its inverse), the memory saved during training is significant.

NOTE: In the main main text we stated a 29 times smaller memory usage for our method. This result was based on an initial analysis that did not take into account the simplification in Equation A1. The results reported here were obtained after the main paper submission deadline, and they will be incorporated in the main text in the revised version.

Table A5: Memory usage comparison between deformation inversion layer and stationary velocity field (SVF) based implementations. The comparison is between executing Equation 5 using deformation inversion layers and executing Equation A1 using SVF integration implementation by Dalca et al. (2018). Between passes memory usage refers to the amount memory needed for storing values between forward and backward passes, and peak memory usage refers to the peak amount of memory needed during forward and backward passes. A volume of shape (256, 256, 256) with 32 bit precision was used. We used 7 scalings and squarings for the SVF integration.

Method	Between passes memory usage (GB) ↓	Peak memory usage (GB) ↓
Deformation inversion layer	0.5625	3.9375
SVF integration	2.8125	4.125

VII Additional results

Figures A2 and A3 visualize dice scores for individual anatomical regions for both OASIS and LPBA40 datasets. VoxelMorph and SYMNet perform systematically worse than our method, while cLapIRN and our method perform very similarly on most regions.

Figure A4 visualizes how the deformation is being gradually updated during the multi-resolution architecture.

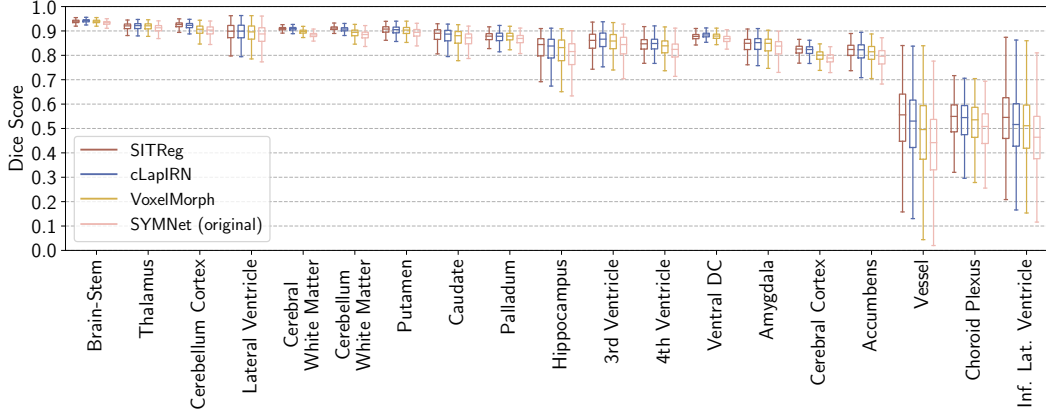


Figure A2: **Individual brain structure dice scores for the OASIS experiment.** Boxplot shows performance of each of the compared methods on each of the brain structures in the OASIS dataset. Algorithms from left to right in each group: SITReg, cLapIRN, VoxelMorph, SYMNet (original)

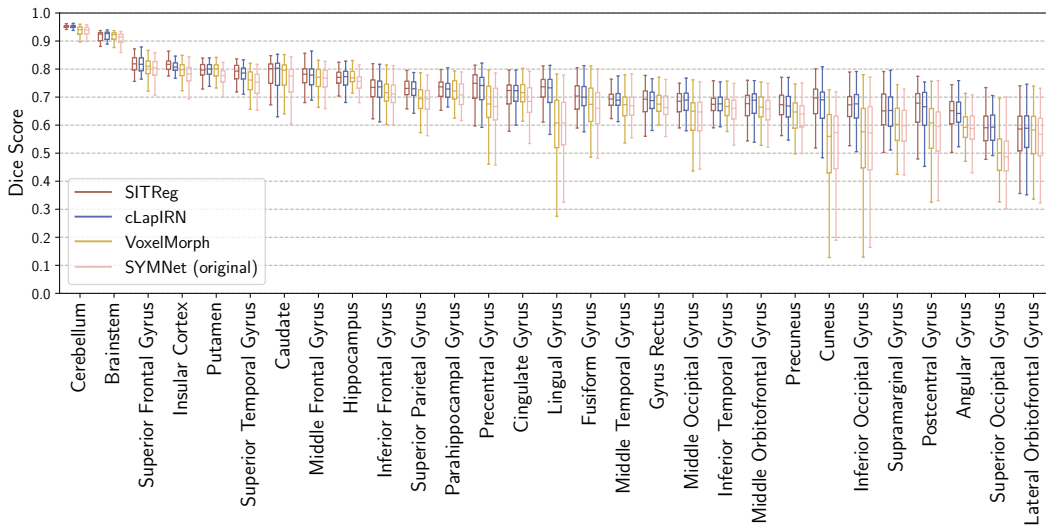


Figure A3: **Individual brain structure dice scores for the LPBA40 experiment.** Boxplot shows performance of each of the compared methods on each of the brain structures in the LPBA40 dataset. Algorithms from left to right in each group: SITReg, cLapIRN, VoxelMorph, SYMNet (original)

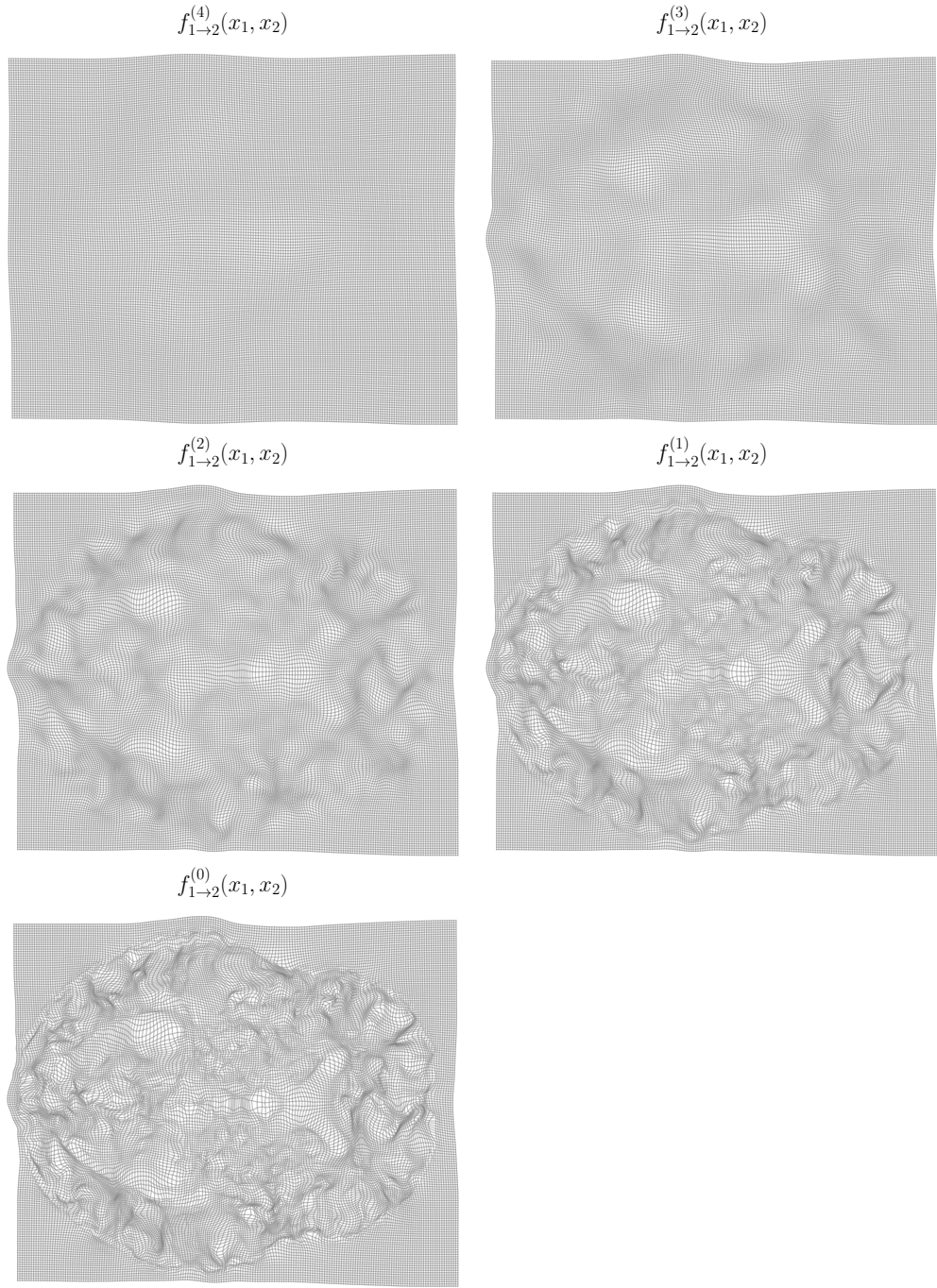


Figure A4: **Visualization of deformation being gradually updated.** Each $f_{1\rightarrow 2}^{(k)}(x_1, x_2)$ corresponds to the full deformation after resolution level k . The example is from the OASIS experiment.

VIII Dataset details

We split the OASIS dataset into 255, 20 and 139 images for training, validation, and testing. The split differs from the Learn2Reg challenge since the test set is not available, but sizes correspond to the splits used by Mok and Chung (2020a,b, 2021). We used all image pairs for testing and validation, yielding 9591 test and 190 validation pairs. For the affinely-aligned OASIS experiment we cropped the images to $144 \times 192 \times 160$ resolution. Images in raw OASIS dataset have resolution $256 \times 256 \times 256$ and we did not crop the images.

We split the LPBA40 into 25, 5 and 10 images for training, validation, and testing. This leaves us with 10 pairs for validation and 45 for testing. We cropped the LPBA40 images to $160 \times 192 \times 160$ resolution.

IX Details on statistical significance

We computed statistical significance of the results comparing the test set predictions of the trained models with each other. We measured the statistical significance using permutation test, and in practice sampled 10000 permutations. In Figures 1 and 2 all the improvements denoted with asterisk (*) obtained very small p-value with not a single permutation (out of the 10000) giving larger mean difference than the one observed.

To establish for certain the relative performance of the methods with respect to the tight metrics, one should train multiple models per method with different random seeds. However, our claim is not that the developed method improves the results with respect to a single tight metric but rather that the overall performance is better by a clear margin (see Section 5).

X Clarifications on symmetry, inverse consistency, and topology preservation

Here we provide examples of symmetry, inverse consistency and lack of topology preservation to further clarify how the terms are used in the paper.

Since symmetry and inverse consistency are quite similar properties, their exact difference might be unclear. Examples of registration methods that are *inverse consistent by construct but not symmetric* are many deep learning frameworks applying the stationary velocity field (Arsigny et al., 2006) approach, e.g, (Dalca et al., 2018; Krebs et al., 2018, 2019; Mok and Chung, 2020a). All of them use a neural network to predict a velocity field for an ordered pair of input images. The final deformation is then produced via Lie algebra exponentiation of the velocity field, that is, by integrating the velocity field over itself over unit time. Details of the exponentiation are not important here but the operation has an interesting property: By negating the velocity field to be exponentiated, the exponentiation results in inverse deformation. Denoting the Lie algebra exponential by \exp , and using notation from Section 1, we can define such methods as

$$\begin{cases} f_{1 \rightarrow 2}(x_1, x_2) &:= \exp(g(x_1, x_2)) \\ f_{2 \rightarrow 1}(x_2, x_1) &:= \exp(-g(x_1, x_2)) \end{cases} \quad (\text{A2})$$

where g is the learned neural network predicting the velocity field. As a result, the methods are inverse consistent since $\exp(g(x_1, x_2)) = \exp(-g(x_1, x_2))^{-1}$ (accuracy is limited by spatial sampling resolution). However, by changing the order of inputs to g , there is no guarantee that $g(x_1, x_2) = -g(x_2, x_1)$ and hence such methods are not symmetric by construct.

MICS (Estienne et al., 2021) is an example of a method which is *symmetric by construct but not inverse consistent*. MICS is composed of two components: encoder, say E , and decoder, say D , both of which are learned. The method can be defined as

$$\begin{cases} f_{1 \rightarrow 2}(x_1, x_2) &:= D(E(x_1, x_2) - E(x_2, x_1)) \\ f_{2 \rightarrow 1}(x_1, x_2) &:= D(E(x_2, x_1) - E(x_1, x_2)). \end{cases} \quad (\text{A3})$$

As a result, the method is symmetric by construct since $f_{1 \rightarrow 2}(x_1, x_2) = f_{2 \rightarrow 1}(x_2, x_1)$ holds exactly. However, there is no architectural guarantee that $f_{1 \rightarrow 2}(x_1, x_2)$ and $f_{2 \rightarrow 1}(x_2, x_1)$ are inverses of each other, and the paper proposes to encourage that using a loss function. In the paper they use such components in multi-steps manner, and as a result the overall architecture is no longer symmetric.

Lack of topology preservation means in practice that the predicted deformation folds on top of itself. An example of such deformation is shown in Figure A5.

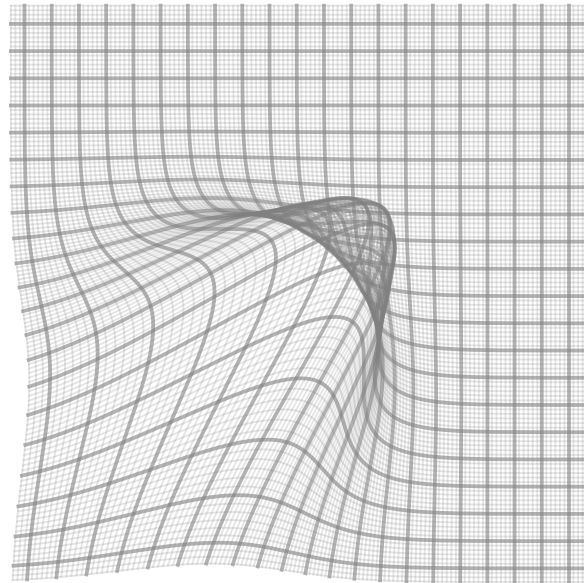


Figure A5: **Visualization of a 2D deformation which is not topology preserving.** The deformation can be seen folding on top of itself.

References

V. Arsigny, O. Commowick, X. Pennec, and N. Ayache. A log-euclidean framework for statistics on diffeomorphisms. In *International Conference on Medical Image Computing and Computer-Assisted Intervention*, pages 924–931. Springer, 2006.

G. Balakrishnan, A. Zhao, M. R. Sabuncu, J. Guttag, and A. V. Dalca. VoxelMorph: A learning framework for deformable medical image registration. *IEEE transactions on medical imaging*, 38(8):1788–1800, 2019.

A. V. Dalca, G. Balakrishnan, J. Guttag, and M. R. Sabuncu. Unsupervised learning for fast probabilistic diffeomorphic registration. In *Medical Image Computing and Computer Assisted Intervention–MICCAI 2018: 21st International Conference, Granada, Spain, September 16–20, 2018, Proceedings, Part I*, pages 729–738. Springer, 2018.

B. D. De Vos, F. F. Berendsen, M. A. Viergever, H. Sokooti, M. Staring, and I. Işgum. A deep learning framework for unsupervised affine and deformable image registration. *Medical image analysis*, 52:128–143, 2019.

T. Estienne, M. Vakalopoulou, E. Battistella, T. Henry, M. Lerousseau, A. Leroy, N. Paragios, and E. Deutsch. MICS: Multi-steps, inverse consistency and symmetric deep learning registration network. *arXiv preprint arXiv:2111.12123*, 2021.

J. Krebs, T. Mansi, B. Mailhé, N. Ayache, and H. Delingette. Unsupervised probabilistic deformation modeling for robust diffeomorphic registration. In *Deep Learning in Medical Image Analysis and Multimodal Learning for Clinical Decision Support*, pages 101–109. Springer, 2018.

J. Krebs, H. Delingette, B. Mailhé, N. Ayache, and T. Mansi. Learning a probabilistic model for diffeomorphic registration. *IEEE transactions on medical imaging*, 38(9):2165–2176, 2019.

T. C. Mok and A. Chung. Fast symmetric diffeomorphic image registration with convolutional neural networks. In *Proceedings of the IEEE/CVF conference on computer vision and pattern recognition*, pages 4644–4653, 2020a.

T. C. Mok and A. Chung. Large deformation diffeomorphic image registration with laplacian pyramid networks. In *International Conference on Medical Image Computing and Computer-Assisted Intervention*, pages 211–221. Springer, 2020b.

T. C. Mok and A. Chung. Conditional deformable image registration with convolutional neural network. In *International Conference on Medical Image Computing and Computer-Assisted Intervention*, pages 35–45. Springer, 2021.

D. Ruijters and P. Thévenaz. GPU prefilter for accurate cubic B-spline interpolation. *The Computer Journal*, 55(1):15–20, 2012.

S. I. Young, Y. Balbastre, A. V. Dalca, W. M. Wells, J. E. Iglesias, and B. Fischl. SuperWarp: Supervised learning and warping on U-Net for invariant subvoxel-precise registration. *arXiv preprint arXiv:2205.07399*, 2022.